ACS NANO

www.acsnano.org

ARTICLE

Complex Arrangement of Orthogonal Nanoscale Columns *via* a Supramolecular Orientational Memory Effect

Mihai Peterca,[†,‡] Mohammad R. Imam,[†] Steven D. Hudson,[§] Benjamin E. Partridge,[†] Dipankar Sahoo,[†,‡] Paul A. Heiney,[‡] Michael L. Klein,[⊥] and Virgil Percec*[,†]

[†]Roy & Diana Vagelos Laboratories, Department of Chemistry, and [‡]Department of Physics and Astronomy, University of Pennsylvania, Philadelphia, Pennsylvania 19104, United States

[§]National Institute of Standards and Technology, Gaithersburg, Maryland 20899, United States

[⊥]Institute of Computational Molecular Science, Temple University, Philadelphia, Pennsylvania 19122, United States

Supporting Information

ABSTRACT: **Memory effects, including shape, chirality, and liquid-crystallinity, have enabled macroscopic materials with novel functions. However, the generation of complex supramolecular nanosystems *via* memory effects has not yet been investigated. Here, we report a cyclotriveratrylene-crown (CTV) compound that self-assembles into supramolecular columns and spheres forming, respectively, hexagonal and cubic mesophases. Upon transition from one phase to the other, an epitaxial relationship holds, *via* an unprecedented supramolecular orientational memory effect. Specifically, the molecular orientation and columnar character of supramolecular packing is preserved in the cubic phase, providing an otherwise inaccessible structure comprising orthogonally oriented domains of supramolecular columns. The continuous columnar character of tetrahedrally distorted supramolecular spheres self-organized from the CTV derivative in the faces of the $Pm\bar{3}n$ lattice is the basis of this supramolecular orientational memory, which holds throughout cycling in temperature between the two phases. This concept is expected to be general for other combinations of periodic and quasiperiodic arrays generated from supramolecular spheres upon transition to supramolecular columns.**

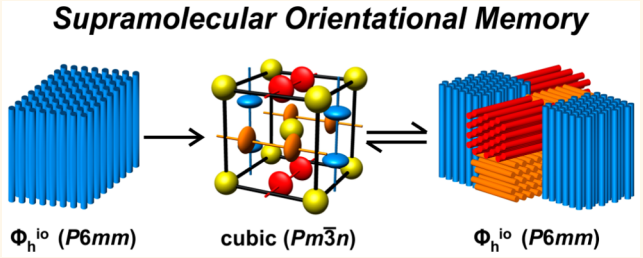

KEYWORDS: *memory effect, complex arrangement, orthogonal columns, supramolecular, self-assembly*

Memory effects, in science and in society at large, allow "a past event [to be] inferred from a present state".[1] Ölander discovered shape memory in AuCd alloys in 1932.[2] Since then, shape memory has been observed in other alloys, in ceramics, and in metals such as titanium.[3−6] Recently, memory effects have been transplanted from hard to soft materials. Shape memory polymers,[7−9] which adopt different macroscopic shapes in response to an external stimulus, have been designed for use as self-tying sutures[10] and for other biomedical applications.[11] Chiral memory refers to the preservation of induced chirality after removal of a chiral inducer,[12−14] whereas orientational memory in nematic liquid crystals[15] has been employed to develop liquid-crystal displays.[16,17] Additional memory effects are expected to provide new complex architectures with novel functions and applications.

Libraries of self-assembling dendrons and dendrimers have been utilized to discover a variety of nanoscale periodic and quasiperiodic arrays self-organized from supramolecular spheres, including $Pm\bar{3}n$ cubic,[18−20] $Im\bar{3}m$ body-centered cubic (bcc),[21] $P4_2/mnm$ tetragonal,[22] and 12-fold liquid-quasicrystalline (LQC).[23] These assemblies were recently generalized for self-organized soft condensed matter including block copolymers and surfactants[24−30] and have been studied computationally.[31−36] In this report, the supramolecular columns generated from a self-assembling cyclotriveratrylene-crown (CTV)[37−39] were discovered to display an unprecedented *supramolecular orientational memory* effect at the transition between columnar hexagonal with intracolumnar order (Φ_h^{io}, *P6mm*) and cubic ($Pm\bar{3}n$) phases. A complex arrangement of orthogonal supramolecular columns, whose orientations are preserved from the cubic phase upon cooling to the columnar hexagonal phase, was observed. This new architecture cannot be constructed by any other methodology

Received: September 22, 2016
Accepted: November 9, 2016
Published: November 9, 2016

DOI: 10.1021/acsnano.6b06419
ACS Nano 2016, 10, 10480−10488

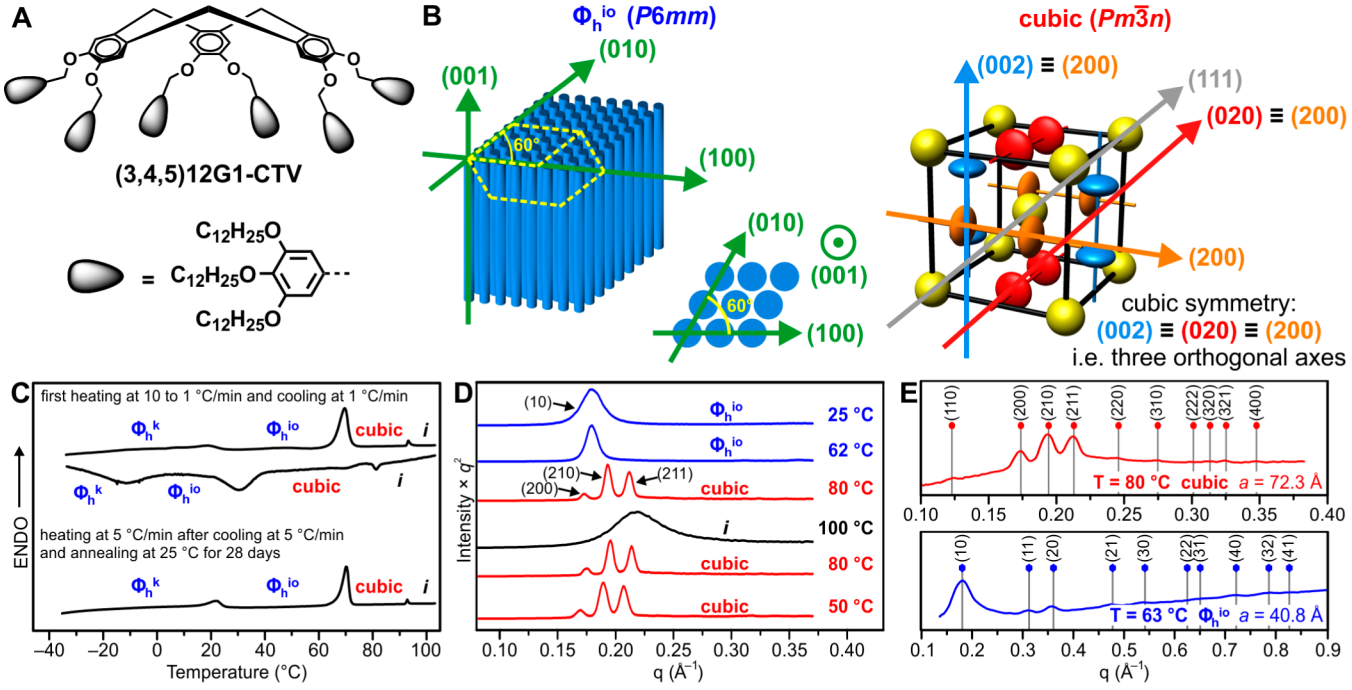

Figure 1. (A) Molecular structure of (3,4,5)12G1-CTV. (B) Schematic representation of columnar hexagonal with intracolumnar order, Φ_h^{io} (*P6mm*) and cubic (*Pm*$\bar{3}$*n*) periodic arrays. In the cubic unit cell, flattened disk-like units represent tetrahedrally distorted supramolecular spheres. (C) DSC traces of (top) first heating and cooling at 10 °C/min and (bottom) heating at 5 °C/min after annealing at 25 °C for 28 days. (D) Small-angle powder XRD plots measured at indicated temperature and phase. (E) Selected wide-angle XRD plots of the (top) cubic (*Pm*$\bar{3}$*n*) and (bottom) Φ_h^{io} (*P6mm*) phases. Vertical lines indicate calculated diffraction peak positions.

except the supramolecular orientational memory introduced here.

RESULTS AND DISCUSSION

Thermal, Structural, and Retrostructural Analysis by Differential Scanning Calorimetry and X-ray Diffraction. The **(3,4,5)12G1-CTV** dendrimer employed (Figure 1A) self-organizes into hexagonal and cubic phases.[37] This organization was enabled by the crown conformation of CTV (Figure 1A), which facilitates packing of the molecules into supramolecular columns and spheres. Thermal and structural analysis by differential scanning calorimetry (DSC) and X-ray diffraction (XRD) on powder and oriented fibers revealed the formation of a columnar hexagonal crystal (Φ_h^k) below 18 °C which transforms into a 2D Φ_h^{io} (*P6mm*) array at 18 °C during first heating and to a cubic (*Pm*$\bar{3}$*n*) lattice above 69 °C (Figure 1B–E). Upon cooling at 1 °C/min, the cubic phase is observed below 56 °C, followed by Φ_h^{io} at 30 °C and Φ_h^k at −12 °C. Faster cooling requires annealing at 25 °C to replicate the phase behavior observed upon initial heating.

Orientational Relationship Observed in XRD Patterns of Oriented Fibers. XRD measurements were made on extruded fibers of **(3,4,5)12G1-CTV** assemblies (Figure 2). Extrusion of the fiber in Φ_h^{io} preferentially aligns the supramolecular columns along the fiber axis, which is the $(001)_{hex}$ direction (Figure 1B).[38] Unexpectedly, an orientational relationship (Supporting Figure S1) was observed, first upon heating from the Φ_h^{io} to the cubic (*Pm*$\bar{3}$*n*) phase and subsequently upon cooling from the cubic to the Φ_h^{io} phase (compare Figure 2A, left and right panels). Such orientational relationships may also be termed "epitaxy" or "epitaxial relationships" to indicate the preservation of certain crystallographic directions upon the indicated phase transition.[40−44]

During a first-order transition between different phases, the new phase often grows from "seeds" within the previous phase, in which case there is no reason for any orientational relationship between the two phases. If such a relationship does exist, one would expect that it would either preserve local structural units or some symmetry feature of the two lattices. In the present case, Φ_h^{io} consists of columns dominated by $\pi-\pi$ interactions between aromatic units which are orthogonal to the column axes,[37] while the cubic (*Pm*$\bar{3}$*n*) phase comprises eight supramolecular spheres (Figure 1B and Supporting Figure S1).[18,19] Columnar hexagonal phases have a single axis with six-fold rotational symmetry, while cubic *Pm*$\bar{3}$*n* lattices have multiple four-fold axes of rotation and four $(111)_{cub}$ axes with three-fold symmetry along the body diagonals of the cube (Figure 1B and Supporting Figure S1). One potential orientational relationship would preserve an axis of three-fold rotational symmetry, *via* alignment of one of the four $(111)_{cub}$ cubic axes (Supporting Figure S1) with the columnar $(001)_{hex}$ axis (Figure 1B and Supporting Figure S1). This particular orientational relationship has been observed in lipids[40−42] and mixtures of block copolymers[43] forming a bicontinuous *Ia*$\bar{3}$*d* cubic phase and in lipids[44] and supramolecular dendrimers[45] forming a *Pm*$\bar{3}$*n* cubic phase. However, no mechanism of this process has been proposed.

An alternative epitaxial relationship would preserve local structural units insofar as possible so that, upon transformation of the cubic phase to the hexagonal phase, adjacent tetrahedrally distorted supramolecular spheres along one of the three $(200)_{cub}$ directions merge to form columns aligned along the $(200)_{cub}$ direction. To our knowledge, this relationship has not been observed in any system to date. Small-angle X-ray scattering (SAXS) oriented fiber measurements (Figure 2A,C) demonstrate that this latter path is obtained in

DOI: 10.1021/acsnano.6b06419
ACS Nano 2016, 10, 10480−10488

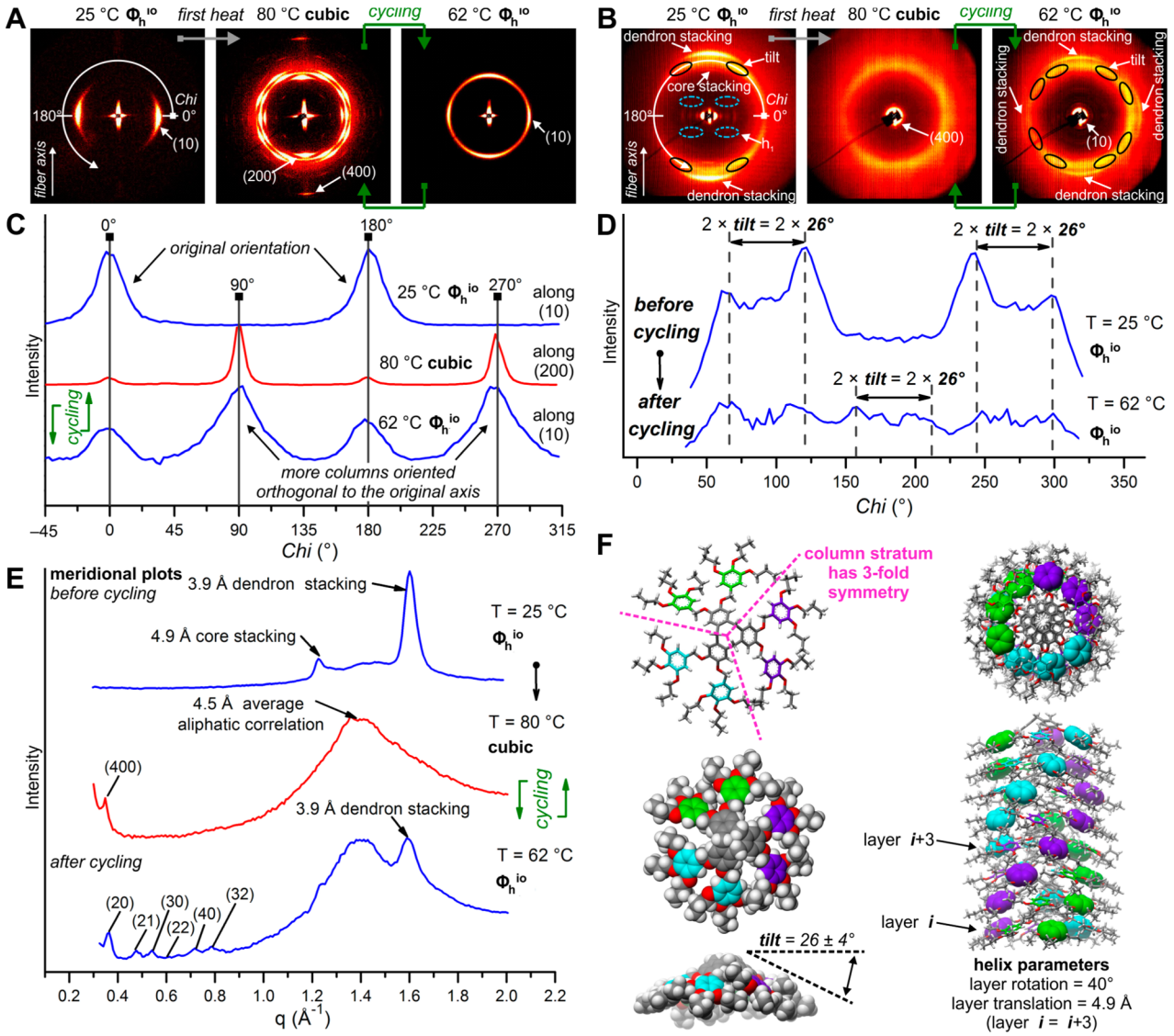

Figure 2. (A) Small-angle X-ray scattering and (B) wide-angle X-ray scattering patterns of (3,4,5)12G1-CTV. (C,D) Azimuthal plots of the patterns in (A) at q_{10} and q_{200} and (B) at q = 1.4 Å^{-1}. (E) Meridional q plots of the patterns in (B). (F) Molecular model of (left) a (3,4,5)12G1-CTV molecule and (right) a supramolecular column self-assembled from (3,4,5)12G1-CTV. Molecular models of the supramolecular sphere are presented in Figure 3D, E.

assemblies of **(3,4,5)12G1-CTV**. Upon heating, the original orientation of the column axis ($(001)_{hex}$) becomes the orientation of nearest-neighbor spheres in the cubic ($Pm\bar{3}n$) phase ($(200)_{cub}$), and upon cooling, supramolecular columns in the Φ_h^{io} phase orient in the direction defined by nearest-neighbor spheres at the face positions of the cubic unit cell, that is, along the $(200)_{cub}$, $(020)_{cub}$, and $(002)_{cub}$ directions (Figure 1B). Hence the orientation of the nearest-neighbor spheres in the cubic phase can be inferred from the orthogonal orientation of the supramolecular columns of the Φ_h^{io} phase. This represents the first example of $(001)_{hex}$ to $(200)_{cub}$ epitaxy (Supporting Figure S1) in a structure organized from a single self-assembling building block.

Wide-angle X-ray scattering (WAXS) fiber and powder experiments (Figure 2B,D,E) provide additional information on the structures self-organized from **(3,4,5)12G1-CTV** in the Φ_h^{io} and cubic ($Pm\bar{3}n$) phases. A strong 3.9 Å feature associated with $\pi-\pi$ stacking correlations between dendrons in Φ_h^{io} is observed both in the original oriented fiber and in a cycled fiber, which was heated to 80 °C and cooled to 25 °C four times (Figure 2B,E). Due to the three-dimensional orthogonal reorientation of the columns, in the cycled fiber, the 3.9 Å $\pi-\pi$ stacking features appear in the equatorial position, as well as in the meridional position. This supports the hypothesis that the supramolecular orientational memory of the hexagonal-to-cubic phase transition is mainly dictated by the strong core−core aromatic interactions which preserve local packing. Core stacking features at 4.9 Å and diffuse off-meridional helical features were identified in the XRD pattern of the original oriented fiber (Figure 2B). This stacking value was used to calculate a density of one molecule per 4.9 Å column stratum in the Φ_h^{io} array (Supporting Table ST1). Tilt features in the original oriented fiber and cycled fiber indicate that the alkyl chains of **(3,4,5)12G1-CTV** are tilted down from the molecular stratum by 26°, in agreement with the expected tilt value of the CTV (Figure 2B,D,F).[37,39] These alkyl chains are melted in the high temperature cubic ($Pm\bar{3}n$) phase, as

DOI: 10.1021/acsnano.6b06419
ACS Nano 2016, 10, 10480−10488

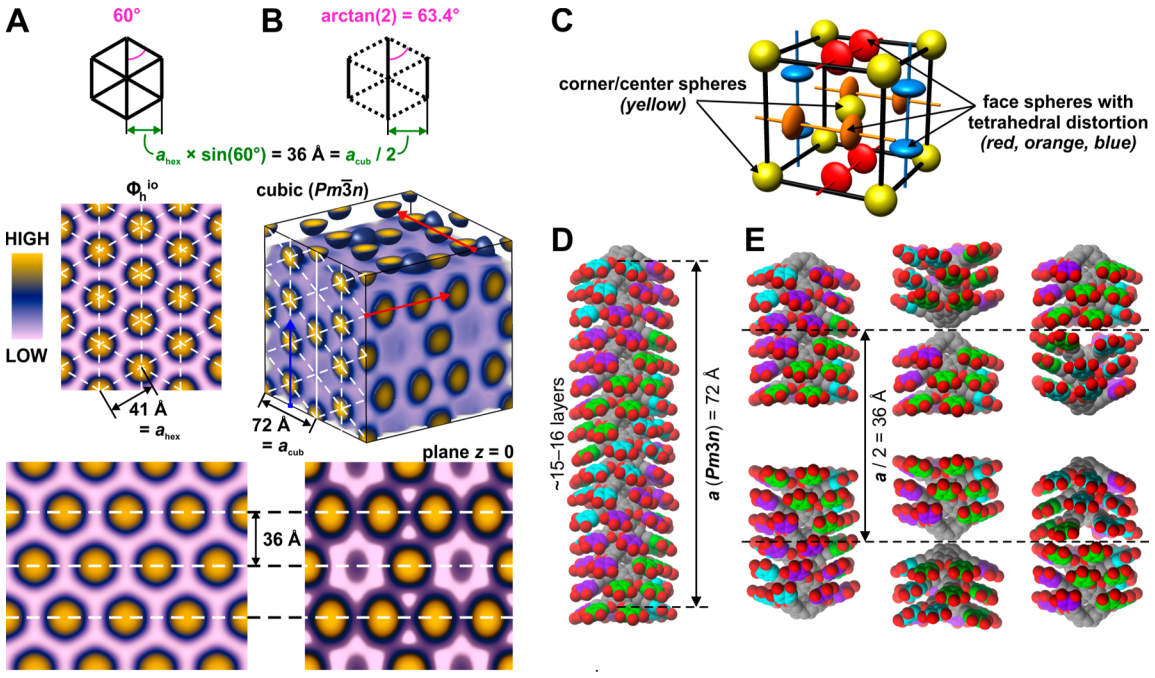

Figure 3. Electron density maps of the (A) Φ_h^{io} and (B) cubic ($Pm\bar{3}n$) phases reconstructed from XRD data. The top of the figure illustrates the pseudohexagonal symmetry adopted during the phase transition. In (B), the three colored arrows point toward the three orthogonal directions with pseudohexagonal symmetry. (C) Schematic representation of face (blue) and center (yellow) tetrahedrally distorted spheres of the $Pm\bar{3}n$ lattice. (D,E) Possible mechanisms of transformation from the supramolecular column (D) to spheres with columnar character in the faces of the cubic phase (E). For simplicity in (D,E), alkyl chains are not shown. Color code: H atoms, white; O atoms, red; C atoms of the dendron aromatic benzyl, green, dark or light blue; all other C atoms, gray.

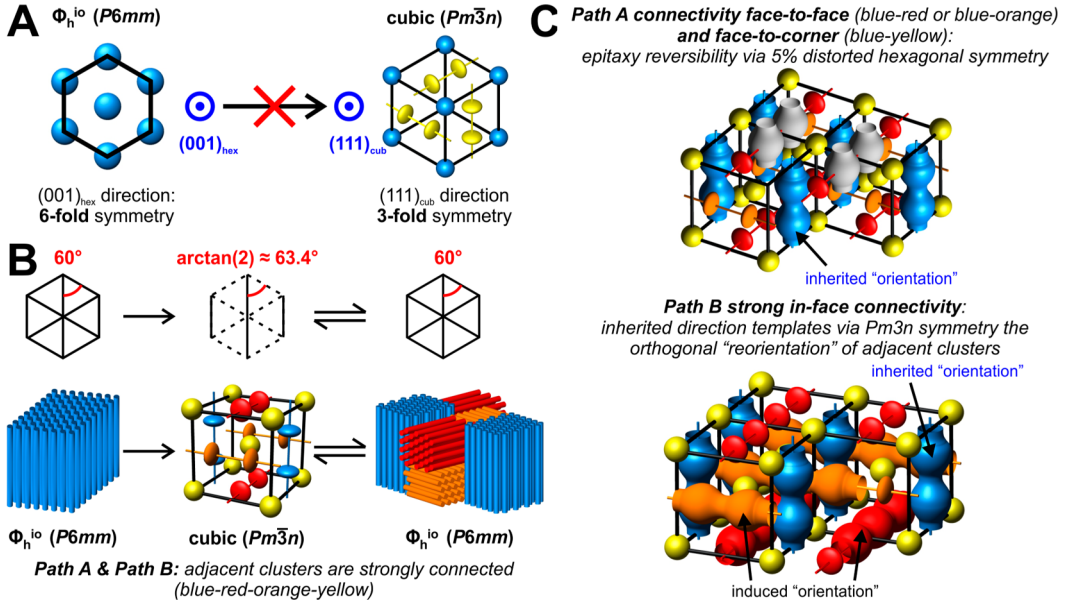

Figure 4. (A) Upon the phase transition, the expected rotational symmetry is broken to conserve the pseudohexagonal and hexagonal symmetries. Color code in (A): blue, original orientation preserved by the corner/center spheres; yellow, face spheres of the cubic phase. (B) Depiction of reorientation of hexagonal microdomains according to the cubic lattice. In the cubic unit cell, flattened disk-like units represent tetrahedrally distorted spheres. (C) Columnar character in the supramolecular spheres of the cubic phase. Color code in (B,C): blue, original orientation; red and orange, columns or spheres "reoriented" in a direction perpendicular to the original one; yellow, center or corner spheres of the cubic phase that can adopt the blue, red, or orange orientation.

indicated by the presence of a broad peak at the 4.5 Å average alkyl chain correlation length (Figure 2E).

These structural results demonstrate that the cycled structure recovers the Φ_h^{io} phase but is oriented in multiple orthogonal directions. The $(001)_{hex}$ axis of the original Φ_h^{io} phase establishes one of three $(200)_{cub}$ directions such that the other $(200)_{cub}$ directions are orthogonally distributed randomly about that axis. Each $(200)_{cub}$ direction then establishes a $(001)_{hex}$ direction in the re-formed Φ_h^{io} phase to produce columnar hexagonal domains aligned along all of the former

DOI: 10.1021/acsnano.6b06419
ACS Nano 2016, 10, 10480−10488

$(200)_{cub}$ directions. The cycled fiber orientation was investigated in both the Φ_h^{io} (fibers monitored at 23 °C over several months) and the $Pm\bar{3}n$ phase (fiber monitored for 3 h at 85 °C), and the preferred orthogonal orientation was found to be stable in time. The data reported in Figure 2 were repeated with different batches of fibers in which the cycling between phases was repeated six times. These fibers were remeasured 3 months later to confirm the stability of the preferred orientation.

Molecular Model of (3,4,5)12G1-CTV. The model for **(3,4,5)12G1-CTV** packing in columns based on SAXS and WAXS powder and oriented fiber data is shown in Figure 2F. Tilt features in oriented XRD patterns (Figure 2B,D) suggest an angle of 26°, consistent with the crown conformation of the CTV (Figure 2F). This intramolecular tilt facilitates stronger interaction between the outer aromatic regions of adjacent molecules (denoted by the 3.9 Å $\pi-\pi$ stacking feature in Figure 2B,E) than between the relatively large CTV of adjacent molecules (denoted by the 4.9 Å separation feature in Figure 2B,E). The helical features at 14.8 Å (Figure 2B), taken with the 4.9 Å separation distance, imply that there are three molecules per repeating unit of the helical column (Figure 2F). Due to the three-fold axis of rotational symmetry in **(3,4,5)12G1-CTV**, this suggests that molecules are rotated by 40° with respect to their neighbor in the column.

The Φ_h^{io} phase comprises cofacially stacked **(3,4,5)12G1-CTV** which maximize aromatic $\pi-\pi$ interactions, while the $Pm\bar{3}n$ phase contains eight supramolecular spheres whose assembly is driven by phase segregation of high electron density aromatic regions and low electron density melted aliphatic domains. This phase segregation is demonstrated by Figure 3A,B, which compares the reconstructed electron density map of the hexagonal Φ_h^{io} phase with the volumetric representation of the electron density of the $Pm\bar{3}n$ phase based on the powder XRD data from Figure 1D (histograms in Supporting Figure S5).

Mechanism of Supramolecular Orientational Memory and Structure of Supramolecular Spheres. The mechanism of the cubic–hexagonal supramolecular orientational memory can be understood by examining the structure of the two phases (Figure 4). The tetrahedrally distorted spheres from the faces of the $Pm\bar{3}n$ lattice[18,20] exhibit columnar character along the three $(200)_{cub}$ directions[18−20] (see orange, red, and blue in Figure 4B). These tetrahedrally distorted spheres[18,20] form pseudohexagonal structures deformed by less than 6% from true hexagonal symmetry (Figure 3A,B). If the path for the orientational memory had been $(001)_{hex}$ to $(111)_{cub}$, as will be reported for other cases, rather than $(001)_{hex}$ to $(200)_{cub}$ as reported here (Figure 1B and Supporting Figure S1), face spheres (Figure 4A, yellow) would require a large translation to integrate into the hexagonal columns. This process would involve substantial disruption to the strong aromatic core interactions. Instead, the tetrahedrally distorted face spheres merge along the $(200)_{cub}$ direction dictated by their continuous columnar character into supramolecular columns (Figure 4C, path A), which shift slightly to form hexagonal symmetry (Figure 4B). In the reverse process, formation of the corner spheres requires only a short translation, while formation of the face spheres requires local reorientations of the molecules but almost no translation of the columns because the lattice parameter of the cubic phase is almost double that of the hexagonal phase (Figure 3A,B).

A simplified way to envision the mechanism of the supramolecular orientational memory effect is to introduce conceptually a noncovalently bonded supramolecular unit containing multiple molecules. The helical features (Figure 2B) demonstrated that the intrinsic three-fold symmetry of the **(3,4,5)12G1-CTV** unit generated a long-range 3_1-helical columnar packing (Figure 2F). It is probable that the high-order rotational symmetry of **(3,4,5)12G1-CTV** coupled with the observed tilt (Figure 2B,F) can generate a supramolecular unit of n dendrimers. The interior of this n-dendrimer unit comprises an interlocked aromatic core defined by the strongly interacting CTV which dictates the well-defined preferential orientational axis of the n-molecule unit at all temperatures (Figure 3E), while the exterior of the n-molecule unit is a "softer" spherical (at high temperature) or "harder" cylindrical (at low temperature) with outer shell formed by alkyl chains. This n-dendrimer unit acts as a single structural entity upon cycling between the two phases: the tetrahedrally distorted spheres recouple into columns at low temperatures and separate back into spheres at high temperatures, while retaining their specific preferred direction at any temperature below the isotropization temperature.

Figure 3D,E depicts two models for the formation of supramolecular spheres with columnar character from the supramolecular columns of **(3,4,5)12G1-CTV**. The supramolecular orientational memory observed by XRD (Figure 2) indicates that molecules are distributed into supramolecular spheres in the cubic phase. The experimental density (ρ = 0.96 g/cm^3 at 20 °C; Supporting Table ST1) and lattice parameters of the $Pm\bar{3}n$ cubic phase (Figure 2) indicate that there are, on average, six dendrimers per supramolecular sphere. This is consistent with three packing models for the aromatic CTV, as shown in Figure 3E. The lattice parameter of the cubic phase (a = 72 Å) represents 15−16 molecules within a column of the Φ_h^{io} phase divided into two distorted spherical units (Figure 3D,E). A possible saddle conformation,[39,46] rather than a crown conformation, for the CTV of the middle dendrimer of the spheres in Figure 3E (center) cannot be excluded. However, the saddle conformation has been demonstrated to be a transient metastable conformation and is therefore unlikely to persist in the supramolecular assemblies.[39,46]

The orientational memory observed in the hexagonal phase on cooling relies on the continuous columnar character of the tetrahedrally distorted spheres from the faces of the cubic phase (Figures 3E and 4C). During the transition from the $Pm\bar{3}n$ to the Φ_h^{io} phase, each of the three $(200)_{cub}$ directions in a given domain is inherited as a $(001)_{hex}$ columnar direction, so that new columnar orientations are established perpendicular to the original direction (Figure 4B). The orientation of the face spheres inherited from the Φ_h^{io} phase (blue in Figure 4B,C) induces orthogonal reorientation in the other two directions (red and orange in Figure 4C). The mechanism *via* which center and corner spheres are integrated into the supramolecular columns is not yet elucidated. Information about the cubic axes can be inferred from the orientation of supramolecular columns in the hexagonal phase, and hence we term this new memory effect *supramolecular orientational memory*.

Visualizing Supramolecular Reorientation by Polarized Birefringence Microscopy. To determine whether the orthogonal reorientation is a local process on the unit cell scale (Figure 4C, path B) or a larger-scale process (Figure 4C, path A), birefringence microscopy experiments were performed (Figure 5A). A thin film in which the supramolecular columns of the hexagonal phase were oriented in the plane of the film (Figure 5A) was heated to 71 °C, where it was held for 1 h

DOI: 10.1021/acsnano.6b06419
ACS Nano 2016, 10, 10480−10488

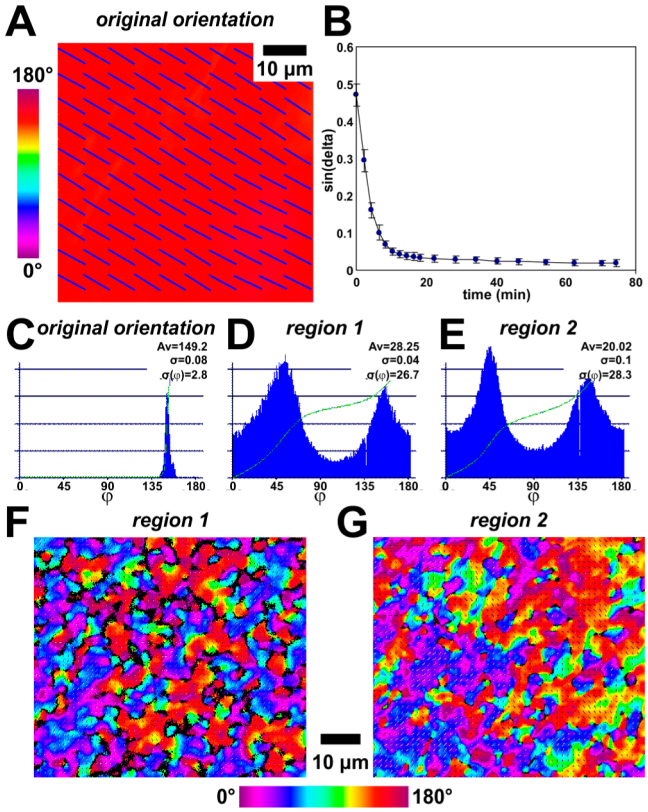

Figure 5. (A) Hexagonal phase after shearing. Columns are nearly uniformly oriented perpendicular to the director lines shown. (B) Decay of birefringence in the cubic phase. (C–E) Orientation distributions of (C) the original film before heating and cooling and (D,E) selected regions of the film after heating and cooling as described in the main text. (F,G) Two representative regions with 90° separated bimodal birefringence in the hexagonal phase after cooling from the cubic phase. Each image (A,F,G) spans 60 μm from top to bottom (scale bars indicated). Color code: orange, original orientation ($\varphi \approx 149°$); blue, second orientation ($\varphi \approx 59°$).

(Figure 5B). It was then heated at 1 °C/min to 75 °C and held for 5 min. After being cooled at 0.4 °C/min to 26 °C and reheated at 2 °C/min to 60 °C, the birefringence was measured. A bimodal orientation with two peaks of comparable intensity separated by 90° orientation was observed (Figure 5D,E). The lack of intermediate orientations is apparent from the dearth of green shades in the orientation maps (Figure 5F,G). One prominent orientation was parallel to the original orientation ($\varphi \sim 149°$) and the other perpendicular ($\varphi \sim 59°$), consistent with a reversible epitaxial relationship between the cubic and columnar phases. The two in-plane columnar orientations arising from epitaxy from the cubic phase are well mixed (Figure 5F), with the proportion of one or the other in a particular neighborhood having some randomness (Figure 5G). The structure coarsens with annealing, while regions of one orientation swallow the other. This behavior signals that columnar orientation, by epitaxy from the cubic, is a local statistically random process, supporting strongly the concept of shared supramolecular arrangement between the cubic and hexagonal phases.

CONCLUSIONS

We have demonstrated that supramolecular spheres self-assembled from **(3,4,5)12G1-CTV**-crown self-organize into Φ_h^{io} ($P6mm$) and cubic ($Pm\bar{3}n$) phases with preferred orientation. The orientational preference of the supramolecular spheres in an aligned Φ_h^{io} is preserved upon heating to $Pm\bar{3}n$ and again upon cooling to Φ_h^{io}, generating a complex architecture featuring orthogonally oriented columnar hexagonal microdomains which cannot be generated through any other mechanism known to us. The only mechanism that explains both the direction and the reversibility of this memory effect invokes the formation of supramolecular tetrahedrally distorted spheres with a preferred orientation. This orientational relationship is introduced here as the concept of supramolecular orientational memory. The supramolecular structural units of materials with supramolecular orientational memory remember their orientations during phase transitions. In the present system, we observe a $(001)_{hex}$ to $(200)_{cub}$ supramolecular orientational memory effect in the assemblies of **(3,4,5)12G1-CTV**. The strong interactions between CTV molecules are preserved by a $(001)_{hex}$ to $(200)_{cub}$ epitaxial relationship and provide a driving force for $(001)_{hex}$ to $(200)_{cub}$ memory rather than the $(001)_{hex}$ to $(111)_{cub}$ relationship to be reported soon and also observed in biphasic mixtures.[40−44] This concept is expected to be elaborated for further $Pm\bar{3}n$ cubic phases known also as Frank-Kasper A15 structures[47] and will be reported soon in other 3D phases generated from spheres, such as $Im\bar{3}m$ bcc cubic,[30] $P4_2/mnm$ tetragonal,[24,29] and LQC[26,28] at their transition to various columnar phases. It is also expected that this concept will be transplanted from self-assembling dendrimers to block copolymers,[24,26,28,29] surfactants,[25] and other soft matter[27,28] displaying this combination of phases. Therefore, supramolecular orientational memory is expected to become a general concept for the creation of otherwise inaccessible complex supramolecular architectures with as yet unknown functions. Novel functions derived from these new complex arrangements of orthogonal columns *via* the supramolecular orientational memory effect reported here are under investigation and will be reported soon.

METHODS

Synthesis of (3,4,5)12G1-CTV. **(3,4,5)12G1-CTV**[37] was synthesized from **(3,4,5)12G1-CH_2OH**[48−50] according to previously reported procedures (Supporting Scheme SS1). The purity and the structure identity of the intermediary and final products were assessed by a combination of techniques that includes thin-layer chromatography, high-pressure liquid chromatography, ^1H and ^{13}C NMR, and matrix-assisted laser desorption/ionization time-of-flight mass spectrometry.

Differential Scanning Calorimetry. Thermal transitions were measured on TA Instruments 2920 modulated and a Q100 differential scanning calorimeter integrated with a refrigerated cooling system. Heating and cooling rates are indicated in Figure 1C. The transition temperatures were measured as the maxima and minima of their endothermic and exothermic peaks. Indium was used as the standard for the calibration.

Density Measurements. For density measurements, a small mass of sample (~0.4 mg) was placed in a vial filled with water followed by ultrasonication to remove the air bubbles embedded within the sample. The sample sank to the bottom of the vial due to its high density compared with water. A saturated aqueous solution of potassium iodide (KI) was then added into the solution at ~0.1 g per aliquot to gradually increase the solution density. KI was added at an interval of at least 20 min to ensure equilibrium within the solution. When the sample was suspended in the middle of the solution, the

DOI: 10.1021/acsnano.6b06419
ACS Nano 2016, 10, 10480−10488

density of the sample was identical to that of the solution, which was measured by a 10 mL volumetric flask.

X-ray Diffraction. XRD measurements were performed using Cu $K\alpha_1$ radiation (λ = 1.542 Å) from a Bruker-Nonius FR-591 rotating anode X-ray source equipped with a 0.2 × 0.2 mm^2 filament and operated at 3.4 kW. Osmic Max-Flux optics and triple pinhole collimation were used to obtain a highly collimated beam with a 0.3 × 0.3 mm^2 spot on a Bruker-AXS Hi-Star multiwire area detector. To minimize attenuation, and background scattering, an integral vacuum was maintained along the length of the flight tube and within the sample chamber. Samples were held in glass capillaries (1.0 mm in diameter), mounted in a temperature-controlled oven (temperature precision = ±0.1 °C, temperature range from −10 to 210 °C). Aligned samples for fiber XRD experiments were prepared using a custom-made extrusion device.[51] The powdered sample (~10 mg) was heated inside the extrusion device. After slow cooling, the fiber was extruded in the liquid-crystal phase and cooled to 23 °C. Typically, the aligned samples had a thickness of 0.3−0.7 mm and a length of 3−7 mm. All XRD measurements were done with the aligned sample axis perpendicular to the beam direction. Primary XRD analysis was performed using Datasqueeze (version 3.0.5).[52]

Molecular Modeling and Simulation. Structural and retrostructural analysis[53,54] was performed *via* molecular modeling and simulation experiments as reported previously.[18,39,55,56] XRD patterns were measured of oriented fiber and powder samples. Diffraction features and lattice parameters obtained using Datasqueeze (version 3.0.5)[52] were used with helical diffraction theory[55] to generate initial molecular and supramolecular models, using Accelrys Materials Studio (versions 3.1 and 5.0). Geometry optimization was performed using the VAMP module. The XRD pattern expected from this model was simulated using Accelrys Cerius.[2] The simulated and experimental XRD patterns were compared, and the supramolecular model was refined.[39] Electron density maps reconstructed from XRD were also used to assess the validity of the proposed supramolecular model (Supporting Figure S3).[18,56] This process of XRD simulation and model refinement was repeated iteratively until the level of agreement between simulated and experimental XRD patterns was agreeable.

Polarized Light Microscopy and Birefringence Measurements. Birefringence measurements were performed with a Metripol birefringence microscope (Oxford Cryosystems), which is based on the Wood and Glazer method.[57] Monochromatic light (λ = 550 nm) is sent through a rotating polarizer into the sample, then through a quarter wave plate and an analyzer into a CCD camera (10 bit Firewire; Scion CFW-1310 M high-resolution; 1360 × 1024 pixels), which measures the light intensity I. Other measured quantities are the phase difference, θ, between two orthogonally polarized components and the orientation angle, ϕ, of the sample's principal axis. I, θ, and ϕ are inter-related:

$$I = \frac{1}{2} I_o[1 + \sin\{2(\omega_{pol}\tau_m - \varphi)\}\sin\theta]$$

I_o is the transmittance, and ω_{pol} and τ_m denote the polarizer's rotational frequency and the measurement time, respectively. A map of the orientation angle ϕ is shown in Figure 5. Checks and calibrations performed on the system included alignment and light intensity uniformity check, assessment of optical path polarization state without the sample, and assessment of the camera's dark noise and linear response from 0 to 80% of its dynamic range. A 40× objective lens (NA = 0.65; magnification = 0.116 μm/pixel) was used.

A few small grains of **(3,4,5)12G1-CTV** were sheared between two microscope coverslips held at approximately 49 °C. Shearing the material thus in the Φ_h^{io} phase produced a high degree of alignment of the columns parallel to the shearing direction. Shearing was continued until the slides easily separated, leaving highly aligned films on each surface (Figure 5A,C). One slide was removed, and the remaining slide was observed during heat treatment. After the sample was held momentarily at 49 °C, it was then heated to 71 °C and the birefringence was monitored. At this temperature, the cubic phase is stable and the birefringence associated with the columnar phase decayed over a period of several minutes (Figure 5B). The sample was then heated to 75 °C and subsequently cooled from 75 °C at 0.4 °C/min to 26 °C and then heated at 2 °C/min to 60 °C and held at that temperature for 2 h. As birefringence returned, the orientation distribution became bimodal (Figure 5D,E), exhibiting two mutually orthogonal column orientations, one being parallel to the original direction.

ASSOCIATED CONTENT

Supporting Information

The Supporting Information is available free of charge on the ACS Publications website at DOI: 10.1021/acsnano.6b06419.

Synthetic scheme, comparison of previous epitaxy relationships, additional electron density maps and histograms (PDF)

AUTHOR INFORMATION

Corresponding Author

*E-mail: percec@sas.upenn.edu.

ORCID

Mihai Peterca: 0000-0002-7247-4008

Benjamin E. Partridge: 0000-0003-2359-1280

Virgil Percec: 0000-0001-5926-0489

Notes

Certain commercial equipment, instruments, or materials are identified in this paper in order to specify the experimental procedure adequately. Such identification is not intended to imply recommendation or endorsement by the National Institute of Standards and Technology, nor is it intended to imply that the materials or equipment identified are necessarily the best available for the purpose.

The authors declare no competing financial interest.

ACKNOWLEDGMENTS

Financial support by the National Science Foundation (DMR-1066116 (V.P.), DMR-1120901 (V.P. and P.A.H.), and OISE-1243313 (V.P.)), the Humboldt Foundation (V.P.), and the P. Roy Vagelos Chair at Penn (V.P.) is gratefully acknowledged. X.Z. acknowledges support from the joint NSF-EPSRC PIRE project "RENEW" (EPSRC Grant EP-K034308). B.E.P. thanks the Howard Hughes Medical Institute for an International Student Research Fellowship.

REFERENCES

(1) Shigeno, M.; Kushida, Y.; Yamaguchi, M. Molecular Switching Involving Metastable States: Molecular Thermal Hysteresis and Sensing of Environmental Changes by Chiral Helicene Oligomeric Foldamers. *Chem. Commun.* **2016**, *52*, 4955−4970.

(2) Ölander, A. An Electrochemical Investigation of Solid Cadmium-Gold Alloys. *J. Am. Chem. Soc.* **1932**, *54*, 3819−3833.

(3) Schurch, K. E.; Ashbee, K. H. G. A Near Perfect Shape-Memory Ceramic Material. *Nature* **1977**, *266*, 706−707.

(4) Swain, M. V. Shape Memory Behaviour in Partially Stabilized Zirconia Ceramics. *Nature* **1986**, *322*, 234−236.

(5) Wenk, H. R.; Kaercher, P.; Kanitpanyacharoen, W.; Zepeda-Alarcon, E.; Wang, Y. Orientation Relations during the α-ω Phase Transition of Zirconium: *In Situ* Texture Observations at High Pressure and Temperature. *Phys. Rev. Lett.* **2013**, *111*, 195701.

(6) Lai, A.; Du, Z.; Gan, C. L.; Schuh, C. A. Shape Memory and Superelastic Ceramics at Small Scales. *Science* **2013**, *341*, 1505−1508.

(7) Lendlein, A.; Jiang, H.; Junger, O.; Langer, R. Light-Induced Shape-Memory Polymers. *Nature* **2005**, *434*, 879−882.

(8) Xie, T. Tunable Polymer Multi-Shape Memory Effect. *Nature* **2010**, *464*, 267−270.

DOI: 10.1021/acsnano.6b06419
ACS Nano 2016, 10, 10480−10488

(9) Shah, A. A.; Schultz, B.; Zhang, W.; Glotzer, S. C.; Solomon, M. J. Actuation of Shape-Memory Colloidal Fibres of Janus Ellipsoids. *Nat. Mater.* **2014**, *14*, 117−124.
(10) Lendlein, A.; Langer, R. Biodegradable, Elastic Shape-Memory Polymers for Potential Biomedical Applications. *Science* **2002**, *296*, 1673−1676.
(11) Sokolowski, W.; Metcalfe, A.; Hayashi, S.; Yahia, L.; Raymond, J. Medical Applications of Shape Memory Polymers. *Biomed. Mater.* **2007**, *2*, S23−S27.
(12) Furusho, Y.; Kimura, T.; Mizuno, Y.; Aida, T. Chirality-Memory Molecule: A D_2-Symmetric Fully Substituted Porphyrin as a Conceptually New Chirality Sensor. *J. Am. Chem. Soc.* **1997**, *119*, 5267−5268.
(13) Yashima, E.; Maeda, K.; Okamoto, Y. Memory of Macromolecular Helicity Assisted by Interaction with Achiral Small Molecules. *Nature* **1999**, *399*, 449−451.
(14) Helmich, F.; Smulders, M. M. J.; Lee, C. C.; Schenning, A. P. H. J.; Meijer, E. W. Effect of Stereogenic Centers on the Self-Sorting, Depolymerization, and Atropisomerization Kinetics of Porphyrin-Based Aggregates. *J. Am. Chem. Soc.* **2011**, *133*, 12238−12246.
(15) Dozov, I.; Nobili, M.; Durand, G. Fast Bistable Nematic Display Using Monostable Surface Switching. *Appl. Phys. Lett.* **1997**, *70*, 1179−1181.
(16) Araki, T.; Buscaglia, M.; Bellini, T.; Tanaka, H. Memory and Topological Frustration in Nematic Liquid Crystals Confined in Porous Materials. *Nat. Mater.* **2011**, *10*, 303−309.
(17) Serra, F.; Buscaglia, M.; Bellini, T. The Emergence of Memory in Liquid Crystals. *Mater. Today* **2011**, *14*, 488−494.
(18) Balagurusamy, V. S. K.; Ungar, G.; Percec, V.; Johansson, G. Rational Design of the First Spherical Supramolecular Dendrimers Self-Organized in a Novel Thermotropic Cubic Liquid-Crystalline Phase and the Determination of Their Shape by X-Ray Analysis. *J. Am. Chem. Soc.* **1997**, *119*, 1539−1555.
(19) Hudson, S. D.; Jung, H.-T.; Percec, V.; Cho, W.-D.; Johansson, G.; Ungar, G.; Balagurusamy, V. S. K. Direct Visualization of Individual Cylindrical and Spherical Supramolecular Dendrimers. *Science* **1997**, *278*, 449−452.
(20) Dukeson, D. R.; Ungar, G.; Balagurusamy, V. S. K.; Percec, V.; Johansson, G. A.; Glodde, M. Application of Isomorphous Replacement in the Structure Determination of a Cubic Liquid Crystal Phase and Location of Counterions. *J. Am. Chem. Soc.* **2003**, *125*, 15974−15980.
(21) Yeardley, D. J. P.; Ungar, G.; Percec, V.; Holerca, M. N.; Johansson, G. Spherical Supramolecular Minidendrimers Self-Organized in an "Inverse Micellar"-Like Thermotropic Body-Centered Cubic Liquid Crystalline Phase. *J. Am. Chem. Soc.* **2000**, *122*, 1684−1689.
(22) Ungar, G.; Liu, Y.; Zeng, X.; Percec, V.; Cho, W.-D. Giant Supramolecular Liquid Crystal Lattice. *Science* **2003**, *299*, 1208−1211.
(23) Zeng, X.; Ungar, G.; Liu, Y.; Percec, V.; Dulcey, A. E.; Hobbs, J. K. Supramolecular Dendritic Liquid Quasicrystals. *Nature* **2004**, *428*, 157−160.
(24) Lee, S.; Bluemle, M. J.; Bates, F. S. Discovery of a Frank-Kasper σ-Phase in Sphere-Forming Block Copolymer Melts. *Science* **2010**, *330*, 349−353.
(25) Perroni, D. V.; Mahanthappa, M. K. Inverse *Pm*3*n* Cubic Micellar Lyotropic Phases from Zwitterionic Triazolium Gemini Surfactants. *Soft Matter* **2013**, *9*, 7919−7922.
(26) Lee, S.; Leighton, C.; Bates, F. S. Sphericity and Symmetry Breaking in the Formation of Frank−Kasper Phases from One Component Materials. *Proc. Natl. Acad. Sci. U. S. A.* **2014**, *111*, 17723−17731.
(27) Huang, M.; Hsu, C.-H.; Wang, J.; Mei, S.; Dong, X.; Li, Y.; Li, M.; Liu, H.; Zhang, W.; Aida, T.; Zhang, W.-B.; Yue, K.; Cheng, S. Z. D. Selective Assemblies of Giant Tetrahedra *via* Precisely Controlled Positional Interactions. *Science* **2015**, *348*, 424−428.
(28) Gillard, T. M.; Lee, S.; Bates, F. S. Dodecagonal Quasicrystalline Order in a Diblock Copolymer Melt. *Proc. Natl. Acad. Sci. U. S. A.* **2016**, *113*, 5167−5172.
(29) Chanpuriya, S.; Kim, K.; Zhang, J.; Lee, S.; Arora, A.; Dorfman, K. D.; Delaney, K. T.; Fredrickson, G. H.; Bates, F. S. Cornucopia of Nanoscale Ordered Phases in Sphere-Forming Tetrablock Terpolymers. *ACS Nano* **2016**, *10*, 4961−4972.
(30) Zhang, W.; Huang, M.; Su, H.; Zhang, S.; Yue, K.; Dong, X.-H.; Li, X.; Liu, H.; Zhang, S.; Wesdemiotis, C.; Lotz, B.; Zhang, W.-B.; Li, Y.; Cheng, S. Z. D. Toward Controlled Hierarchical Heterogeneities in Giant Molecules with Precisely Arranged Nano Building Blocks. *ACS Cent. Sci.* **2016**, *2*, 48−54.
(31) Ziherl, P.; Kamien, R. D. Maximizing Entropy by Minimizing Area: Towards a New Principle of Self-Organization. *J. Phys. Chem. B* **2001**, *105*, 10147−10158.
(32) Li, Y.; Lin, S.-T.; Goddard, W. A., III Efficiency of Various Lattice from Hard Ball to Soft Ball; Theoretical Study of Thermodynamic Properties of Dendrimer Liquid Crystal from Atomistic Simulation. *J. Am. Chem. Soc.* **2004**, *126*, 1872−1885.
(33) Lifshitz, R.; Diamant, H. Soft Quasicrystals − Why are They Stable? *Philos. Mag.* **2007**, *87*, 3021−3030.
(34) Barkan, K.; Diamant, H.; Lifshitz, R. Stability of Quasicrystals Composed of Soft Isotropic Particles. *Phys. Rev. B: Condens. Matter Mater. Phys.* **2011**, *83*, 172201.
(35) Iacovella, C. R.; Keys, A. S.; Glotzer, S. C. Self-Assembly of Soft-Matter Quasicrystals and their Approximants. *Proc. Natl. Acad. Sci. U. S. A.* **2011**, *108*, 20935−20940.
(36) Engel, M.; Damasceno, P. F.; Phillips, C. L.; Glotzer, S. C. Computational Self-Assembly of a One-Component Icosahedral Quasicrystal. *Nat. Mater.* **2015**, *14*, 109−116.
(37) Percec, V.; Imam, M. R.; Peterca, M.; Wilson, D. A.; Heiney, P. A. Self-Assembly of Dendritic Crowns into Chiral Supramolecular Spheres. *J. Am. Chem. Soc.* **2009**, *131*, 1294−1304.
(38) Percec, V.; Imam, M. R.; Peterca, M.; Wilson, D. A.; Graf, R.; Spiess, H. W.; Balagurusamy, V. S. K.; Heiney, P. A. Self-Assembly of Dendronized Triphenylenes into Helical Pyramidal Columns and Chiral Spheres. *J. Am. Chem. Soc.* **2009**, *131*, 7662−7677.
(39) Roche, C.; Sun, H.-J.; Prendergast, M. E.; Leowanawat, P.; Partridge, B. E.; Heiney, P. A.; Araoka, F.; Graf, R.; Spiess, H. W.; Zeng, X.; Ungar, G.; Percec, V. Homochiral Columns Constructed by Chiral Self-Sorting During Supramolecular Helical Organization of Hat-Shaped Molecules. *J. Am. Chem. Soc.* **2014**, *136*, 7169−7185.
(40) Rancon, Y.; Charvolin, J. Epitaxial Relationships during Phase Transformations in a Lyotropic Liquid Crystal. *J. Phys. Chem.* **1988**, *92*, 2646−2651.
(41) Clerc, M.; Levelut, A. M.; Sadoc, J. F. Transitions between Mesophases Involving Cubic Phases in the Surfactant-Water Systems. Epitaxial Relations and Their Consequences in a Geometrical Framework. *J. Phys. II* **1991**, *1*, 1263−1276.
(42) Sakya, P.; Seddon, J. M.; Templer, R. H.; Mirkin, R. J.; Tiddy, G. J. T. Micellar Cubic Phases and Their Structural Relationships: The Nonionic Surfactant System $C_{12}EO_{12}$/Water. *Langmuir* **1997**, *13*, 3706−3714.
(43) Koppi, K. A.; Tirrell, M.; Bates, F. S.; Almdal, K.; Mortensen, K. Epitaxial Growth and Shearing of the Body Centered Cubic Phase in Diblock Copolymer Melts. *J. Rheol.* **1994**, *38*, 999−1027.
(44) Mariani, P.; Amaral, L. Q.; Saturni, L.; Delacroix, H. Hexagonal-Cubic Phase Transitions in Lipid Containing Systems: Epitaxial Relationships and Cylinder Growth. *J. Phys. II* **1994**, *4*, 1393−1416.
(45) Peterca, M.; Imam, M. R.; Leowanawat, P.; Rosen, B. M.; Wilson, D. A.; Wilson, C. J.; Zeng, X.; Ungar, G.; Heiney, P. A.; Percec, V. Self-Assembly of Hybrid Dendrons into Doubly Segregated Supramolecular Polyhedral Columns and Vesicles. *J. Am. Chem. Soc.* **2010**, *132*, 11288−11305.
(46) Zimmermann, H.; Tolstoy, P.; Limbach, H. H.; Poupko, R.; Luz, Z. The Saddle Form of Cyclotriveratrylene. *J. Phys. Chem. B* **2004**, *108*, 18772−18778.
(47) Klein, M. L.; Levesque, D.; Weis, J.-J. Molecular-Dynamics Study of Solid γ-O_2. *Phys. Rev. B: Condens. Matter Mater. Phys.* **1980**, *21*, 5785−5792.
(48) Percec, V.; Cho, W.-D.; Mosier, P. E.; Ungar, G.; Yeardley, D. J. P. Structural Analysis of Cylindrical and Spherical Supramolecular

DOI: 10.1021/acsnano.6b06419
ACS Nano 2016, 10, 10480−10488

Dendrimers Quantifies the Concept of Monodendron Shape Control by Generation Number. *J. Am. Chem. Soc.* **1998**, *120*, 11061−11070.
(49) Percec, V.; Cho, W. D.; Ungar, G. Increasing the Diameter of Cylindrical and Spherical Supramolecular Dendrimers by Decreasing the Solid Angle of Their Monodendrons *via* Periphery Functionalization. *J. Am. Chem. Soc.* **2000**, *122*, 10273−10281.
(50) Percec, V.; Cho, W.-D.; Ungar, G.; Yeardley, D. J. P. From Molecular Flat Tapers, Discs, and Cones to Supramolecular Cylinders and Spheres Using Fréchet-Type Monodendrons Modified on Their Periphery. *Angew. Chem., Int. Ed.* **2000**, *39*, 1597−1602.
(51) Percec, V.; Sun, H.-J.; Leowanawat, P.; Peterca, M.; Graf, R.; Spiess, H. W.; Zeng, X.; Ungar, G.; Heiney, P. A. Transformation from Kinetically into Thermodynamically Controlled Self-Organization of Complex Helical Columns with 3D Periodicity Assembled from Dendronized Perylene Bisimides. *J. Am. Chem. Soc.* **2013**, *135*, 4129−4148.
(52) Heiney, P. A. *Datasqueeze*: A Software Tool for Powder and Small-Angle X-ray Diffraction Analysis; Commission on Powder Diffraction Newsletter, 2005; Vol. *32*, pp 9−11.
(53) Rosen, B. M.; Wilson, C. J.; Wilson, D. A.; Peterca, M.; Imam, M. R.; Percec, V. Dendron-Mediated Self-Assembly, Disassembly, and Self-Organization of Complex Systems. *Chem. Rev.* **2009**, *109*, 6275−6540.
(54) Sun, H.-J.; Zhang, S.; Percec, V. From Structure to Function *via* Complex Supramolecular Dendrimer Systems. *Chem. Soc. Rev.* **2015**, *44*, 3900−3923.
(55) Peterca, M.; Percec, V.; Imam, M. R.; Leowanawat, P.; Morimitsu, K.; Heiney, P. A. Molecular Structure of Helical Supramolecular Dendrimers. *J. Am. Chem. Soc.* **2008**, *130*, 14840−14852.
(56) Wu, Y.-C.; Leowanawat, P.; Sun, H.-J.; Partridge, B. E.; Peterca, M.; Graf, R.; Spiess, H. W.; Zeng, X.; Ungar, G.; Hsu, C.-S.; Heiney, P. A.; Percec, V. Complex Columnar Hexagonal Polymorphism in Supramolecular Assemblies of a Semifluorinated Electron-Accepting Naphthalene Bisimide. *J. Am. Chem. Soc.* **2015**, *137*, 807−819.
(57) Wood, I. G.; Glazer, A. M. Ferroelastic Phase Transition in $BiVO_4$. I. Birefringence Measurements Using the Rotating-Analyser Method. *J. Appl. Crystallogr.* **1980**, *13*, 217−223.

DOI: 10.1021/acsnano.6b06419
ACS Nano 2016, 10, 10480−10488

Supporting Information for

Complex Arrangement of Orthogonal Nanoscale Columns *via* a Supramolecular Orientational Memory Effect

Mihai Peterca,[†,‡] Mohammad R. Imam, [†] Steven D. Hudson,[§] Benjamin E. Partridge,[†] Dipankar Sahoo,[†,‡] Paul A. Heiney,[‡] Michael L. Klein,[¶] and Virgil Percec*[,†]

[†]Roy & Diana Vagelos Laboratories, Department of Chemistry, University of Pennsylvania, Philadelphia, Pennsylvania 19104-6323, United States

[‡]Department of Physics and Astronomy, University of Pennsylvania, Philadelphia, Pennsylvania 19104-6396, United States

[§]National Institute of Standards and Technology, Gaithersburg, MD 20899-8544, United States

[¶]Institute of Computational Molecular Science, Temple University, Philadelphia, PA 19122.

*E-mail: percec@sas.upenn.edu

Table of Contents

Supporting Scheme SS1. Synthesis of (3,4,5)12G1-CTV

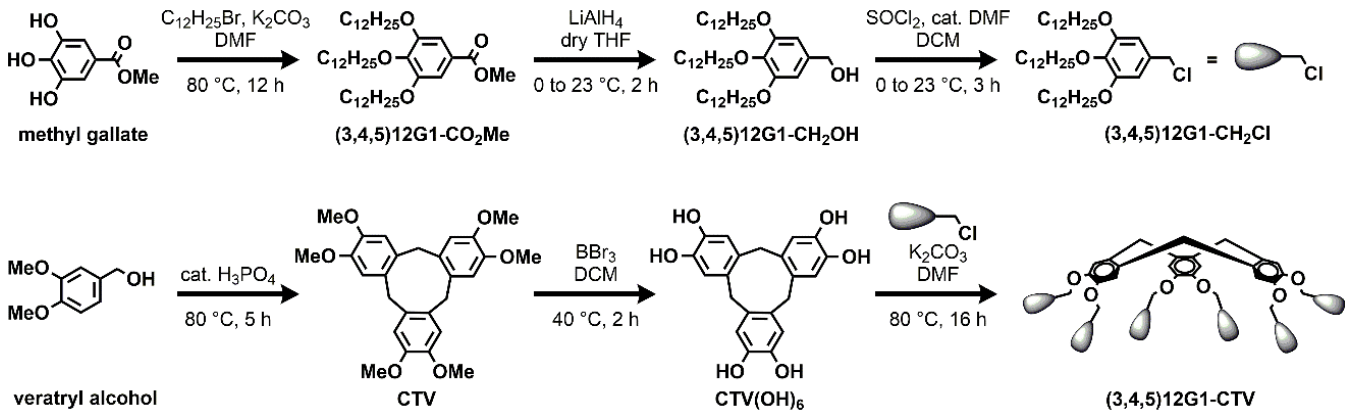

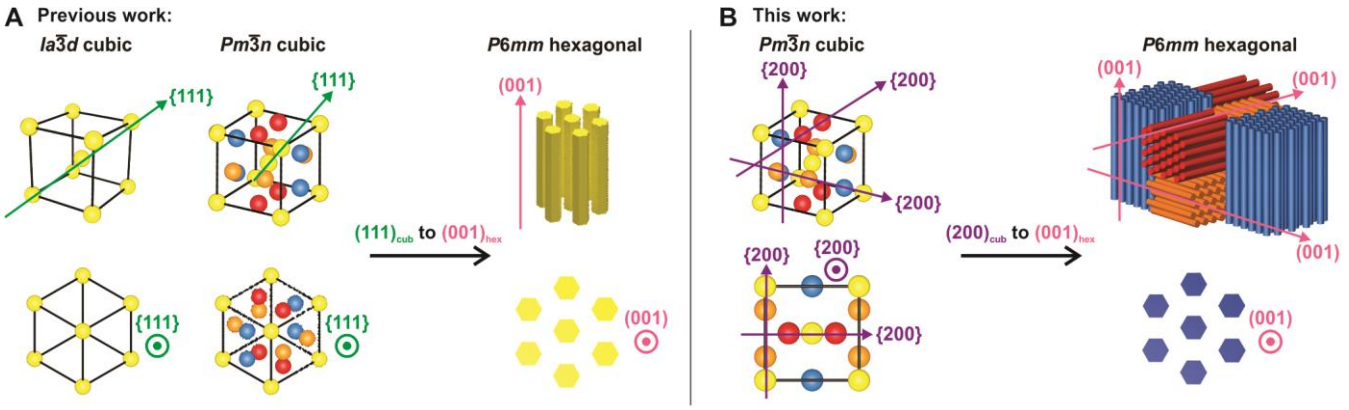

Supporting Figure S1. Comparison of orientational relationships observed in (A) previously reported *Ia*$\bar{3}$*d* and *Pm*$\bar{3}$*n* cubic phases with (B) the current *Pm*$\bar{3}$*n* cubic phase.

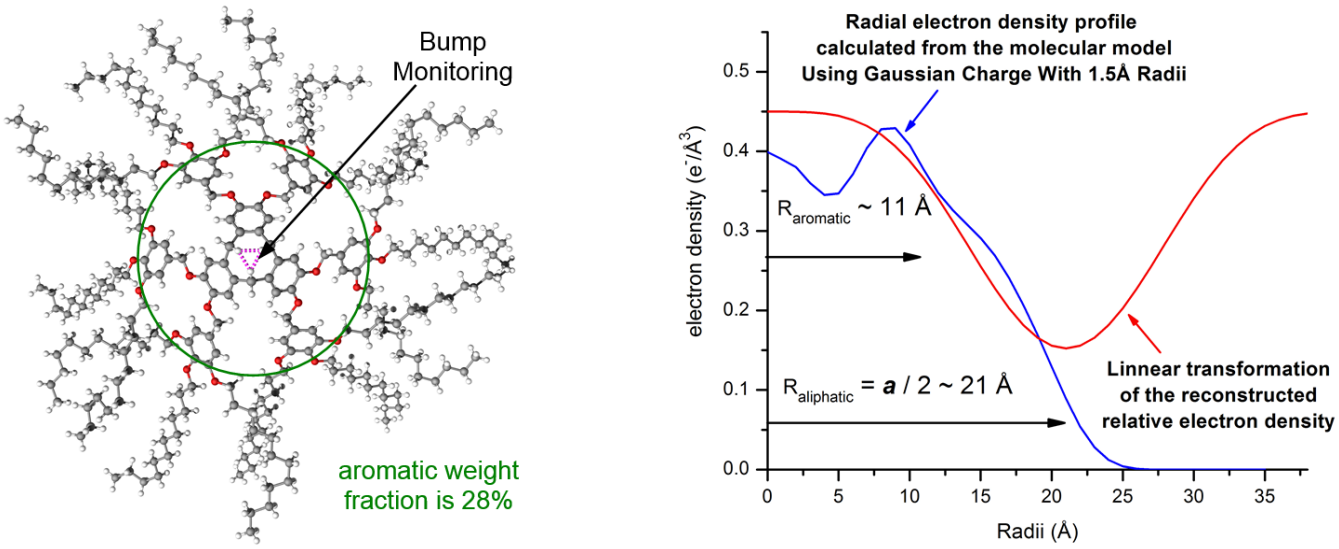

Supporting Figure S2. Comparison of the electron density profile in the columnar hexagonal phase based on the molecular model shown and the one calculated from the X-ray powder diffraction data.

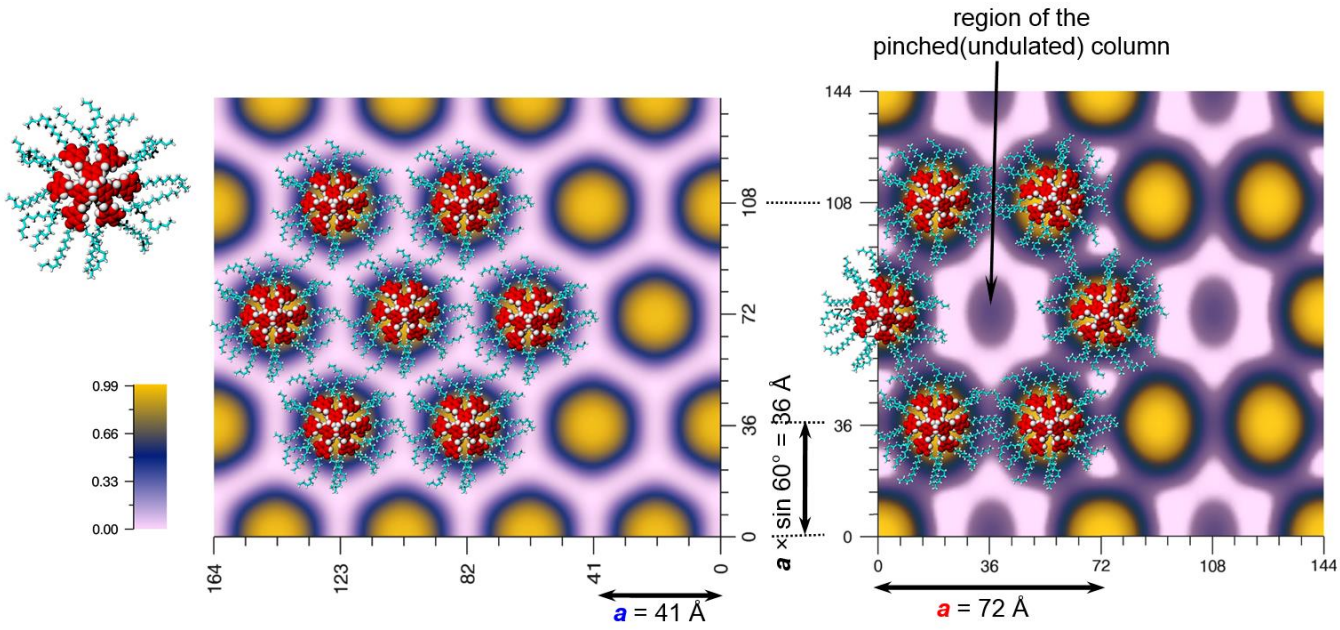

Supporting Figure S3. Molecular model overlaid to scale on the reconstructed relative electron density maps of the hexagonal phase (a) and of the z = 0 plane of the cubic phase (b). Color code: for the molecular model the aromatic region is red and the aliphatic region blue; for the electron density map the high electron density region is yellow. The periphery of the spheres in columnar and cubic phase is filled via interdigitation and trans-gauche conformation of the alkyl region. We remark that the aliphatic region accounts for the 72% the compound molecular weight.

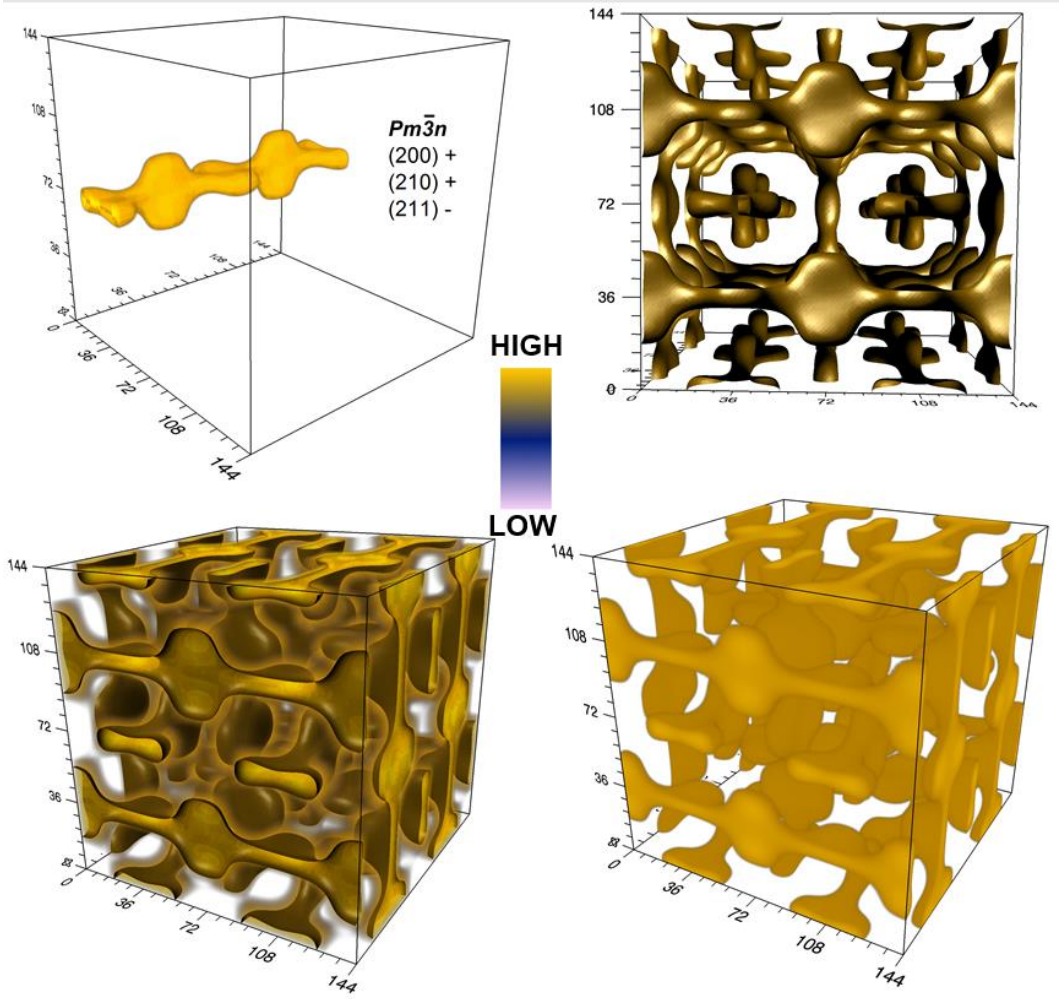

Supporting Figure S4. Alternative electron density solution: the histogram does not fit the expected aromatic to aliphatic electron density distribution (Supporting Figure S5C). In addition, the shape of the high electron density region is twisted, generating frustration of the large aromatic core packing.

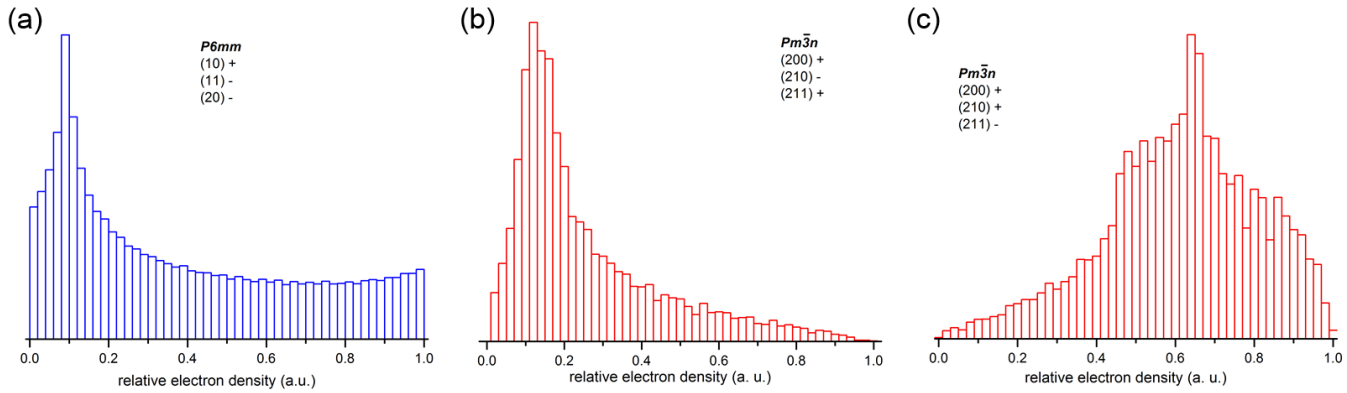

Supporting Figure S5. Histograms of the electron density distribution using the indicated sign of the diffraction peak amplitudes: (a) calculated for the hexagonal phase from the two-dimensional reconstructed relative electron density; (b, c) calculated for the cubic phase using the three-dimensional distribution of the relative electron density in the unit cell. The presence in (c) of a large distribution toward the higher value of the electron density was used to eliminate this choice. The structure has approximately 28% weight of aromatic, thus the region with high electron density is expected to not dominate the distribution.

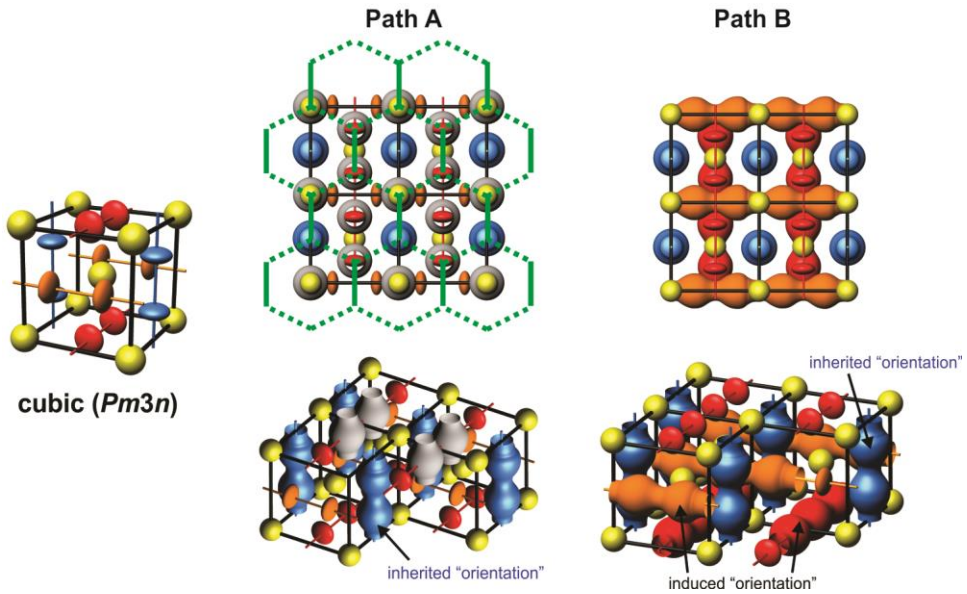

Supporting Figure S6. Columnar character in the supramolecular spheres of the cubic phase. Diagrams show the lattice of the cubic phase from top view. Path A and B correspond to two mechanisms for supramolecular orientation memory as introduced in Figure 4. Color code: blue–original orientation; red and orange–columns or spheres "reoriented" in a direction perpendicular to the original one; yellow–center or corner spheres of the cubic phase that can adopt the blue, red or orange orientation.

Supporting Table ST1. Structural and Retrostructural Analysis of (3,4,5)12G1-CTV

T (°C)	phase [a]	d_{10}, d_{11}, d_{20} [b] d_{200}, d_{210}, d_{211} [c]	A_{10}, A_{11}, A_{20} [d] A_{200}, A_{210}, A_{211} [e]	a [f] (Å)	ρ_{20} [g] (g/cm^3)	μ [h]
62	Φ_h^{io}	34.9, 20.2, 17.5 [b]	79.1, 1.05, 12.7 [d]	40.8	0.96	0.99
80	$Pm\bar{3}n$	35.9, 32.1, 29.4 [c]	24.2, 30.6, 26.4 [e]	72.3	0.96	6.56

[a] $\Phi_{h,io}$ – columnar hexagonal phase with intracolumnar long range order, $Pm\bar{3}n$ – cubic phase;
[b] d_{hk} – d-spacing of the (hk0) reflection of Φ_h^{io}
[c] d_{hkl} – d-spacing of the (hkl) reflection of $Pm\bar{3}n$
[d] A_{hk} – scaled Lorentz-corrected amplitude of the (hk0) reflection of Φ_h^{io} calculated from the diffraction peak area and corrected for multiplicity
[e] A_{hk} – scaled Lorentz-corrected amplitude of the (hkl) reflection of $Pm\bar{3}n$ calculated from the diffraction peak area and corrected for multiplicity
[f] a – lattice parameter calculated for Φ_h^{io} using $a = 2\left(d_{10} + \sqrt{3}d_{11} + \sqrt{4}d_{20}\right)/\left(3\sqrt{3}\right)$, and for $Pm\bar{3}n$ using $a = \left(\sqrt{4}d_{200} + \sqrt{5}d_{210} + \sqrt{6}d_{211}\right)/3$
[g] ρ_{20} – experimental density measured at 20 °C
[h] μ – for Φ_h^{io} the average number of dendrimers per column stratum calculated using $\mu = \left(\sqrt{3}N_A a^2 t \rho_{20}\right)/(2M)$ where t = 4.94 Å is the average column strata thickness, and for $Pm\bar{3}n$ the average number of dendrimers per supramolecular sphere calculated using $\mu = a^3 \rho N_A/(8M)$; in both cases, N_A = Avogadro's number = 6.022×10^{23} mol^{-1}, and M = molecular weight of the dendrimer = 4224.9 g/mol.